Multiscale Modelling of Heat Transfer in Selective Laser Sintering

E. Spangsberg[a], J. Hesselvig[a], R. T. Nygaard[a], M. K. Budzik[a], M. Sandberg[a,*]

[a]*Department of Mechanical and Production Engineering, Aarhus University, DK-8200 Aarhus N, Denmark*

Abstract

This study investigates heat transfer mechanisms in Selective Laser Sintering through a multiscale modeling approach. At the micro-scale, the model simulates heat transfer within a single layer and scan line, capturing laser-powder interactions, phase transformations, and temperature-dependent material properties. At the part scale, two approaches are explored: one with a continuously operating laser and another where the laser heat is applied in discrete bursts, simulating a non-continuous process. Micro-scale results demonstrate rapid thermal responses over millisecond timescales, while the part-scale model reveals slower heating rates to achieve comparable temperatures. The part-scale model with the non-continuous approach also highlights the effects of energy migration across multiple layers. Parameter studies emphasize the sensitivity of thermal profiles to laser operation parameters and layer configurations in the model, with the non-continuous approach producing higher localized temperatures at low laser activation times. Overall, the models provide a numerical framework to optimize SLS processes and deepen the understanding of thermal dynamics during sintering.

Contents

1 Introduction **2**
1.1 Approach . . . 3

2 Micro-Scale Modeling **3**
2.1 Theory . . . 3
2.1.1 Heat transfer equation . . . 3
2.1.2 Phase Transformation . . . 4
2.1.3 Laser Beam Model . . . 7
2.2 Method . . . 8
2.2.1 Boundary Condition Implementation . . . 8
2.2.2 State Variables and Phase Transitions . . . 8
2.2.3 Mesh Generation and Optimization . . . 9
2.2.4 Solver Configuration and Convergence . . . 10
2.2.5 Parameters . . . 10

3 Part Scale Modeling **11**
3.1 Theory . . . 11

*Corresponding author
Email address: ms@mpe.au.dk (M. Sandberg)
Preprint submitted to engrXiv (Engineering Archive)

3.1.1 Addition of Layers . . . 11
3.1.2 Heat Transfer Equation . . . 12
3.1.3 Laser Source Model . . . 13
3.1.4 Phase Transformation . . . 15
3.1.5 Duty Cycle . . . 17
3.2 Method . . . 17
3.2.1 Domain Representation and Meshing . . . 17
3.2.2 Solver Configurations and Duty Cycle . . . 18
3.2.3 Parameters . . . 18

4 Analysis & Discussion **18**
4.1 Presentation of Results . . . 19
4.1.1 Micro-Scale . . . 19
4.1.2 Part Scale . . . 20
4.2 Parameter Studies . . . 22
4.2.1 Activation Time . . . 22
4.2.2 Fusion of Layers . . . 24
4.3 Extension from 2D to 3D Modeling . . . 24
4.4 Uncertainties . . . 25

5 Conclusion **25**

6 Bibliography **26**

1. Introduction

In Additive Manufacturing (AM), components are produced by successively adding material layer by layer, enabling the rapid fabrication of parts designed using computer-aided design (CAD) software. For many years, production companies have utilized this technique for rapid prototyping (RP), allowing them to test new products without requiring a full production line. This approach significantly reduces both time and cost in the iterative design process of developing new products. As AM technologies have advanced, some branches, such as Selective Laser Sintering (SLS), have evolved beyond prototyping to support small-scale production of end-use parts [1].

SLS, a Powder Bed Fusion (PBF) technique, offers several advantages over conventional manufacturing processes, including the ability to produce intricate geometries, minimize material waste, and provide cost-effective solutions for low-volume production [1]. The SLS process uses a laser to fuse polymer powder particles within a powder bed, which is incrementally lowered as each layer is completed and fresh powder is deposited. This approach enables the fabrication of three-dimensional (3D) objects directly from CAD designs. Despite these advantages, the use of SLS for end-use parts remains relatively new compared to traditional methods such as injection molding, which benefits from an extensive body of knowledge for addressing production defects. Further empirical research is required to better understand and mitigate defects in SLS, ensuring the production of consistently high-quality parts.

Due to the complexity of the SLS process, relying solely on experimental observations is often insufficient. Developing numerical models on multiple scales becomes essential for gaining deeper insight into the process [2]. Micro-scale models are critical for understanding fundamental sintering mechanisms, such as the interaction between the laser beam and powder material, as well as the phase change happening in the material. However, micro-scale models are insufficient for predicting overall heat transfer in a whole part, which is crucial for the

quality of the printed part. For this, part-scale models can help in understanding key considerations such as part placement, which greatly affects the heat transfer in and around the printed part. Together, these models enable the development of an optimized SLS process.

1.1. Approach

This report presents a framework for modeling heat transfer in SLS, addressing both the micro-scale and part scale. At the micro-scale, a continuum approach is employed to simulate a single layer and scan line, providing insights into the fundamental heat transfer mechanisms in SLS. At the part scale, the focus is on capturing the thermal behavior of multiple layers and their effect throughout the printing process. By developing numerical frameworks at these two distinct scales, this report aims to provide insights that will contribute to optimizing the SLS process.

2. Micro-Scale Modeling

This chapter focuses on the theoretical framework and approach for simulating the heat transfer mechanisms at the micro-scale.

2.1. Theory

In this section, theory required to successfully model the SLS process will be presented. The section will describe the underlying physics and equations necessary to accurately predict temperature and density distributions in sintered semi-crystalline polymer powders.

To model heat transfer during the SLS process at the micro-scale, it is essential to consider the following factors [3, 4]:

1. Heat transfer mechanisms within the powder and solid material,
2. Phase transformation from powder to solid during the sintering process,
3. Interactions between the laser beam and the powder bed.

2.1.1. Heat transfer equation

The heat transfer mechanisms during the SLS process can be described by the heat conduction equation [3, 5]:

$$\rho C_p^\star \frac{\partial T}{\partial t} = \frac{\partial}{\partial x}\left(k\frac{\partial T}{\partial x}\right) + \frac{\partial}{\partial y}\left(k\frac{\partial T}{\partial y}\right) + \frac{\partial}{\partial z}\left(k\frac{\partial T}{\partial z}\right) + \dot{q}_V$$

which can be written in compact form as:

$$\rho C_p^\star \frac{\partial T}{\partial t} + \nabla \cdot (-k\nabla T) = \dot{q}_V \tag{1}$$

In (1), ρ is the material density $[\mathrm{kg/m^3}]$, $C_p^\star$ is the specific heat capacity of the material $[\mathrm{J/kgK}]$, k is the thermal conductivity $[\mathrm{W/mK}]$, and $\dot{q}_V$ represents the volumetric thermal input from the laser $[\mathrm{W/m^3}]$.

During the SLS process, the top of the powder bed is heated to the processing temperature, T_0, before exposure to the laser [4].

Therefore, it is assumed that prior to sintering, the temperature is uniform throughout the top powder bed layer. The initial condition is defined as:

$$T(x, y, z, 0) = T_0 \tag{2}$$

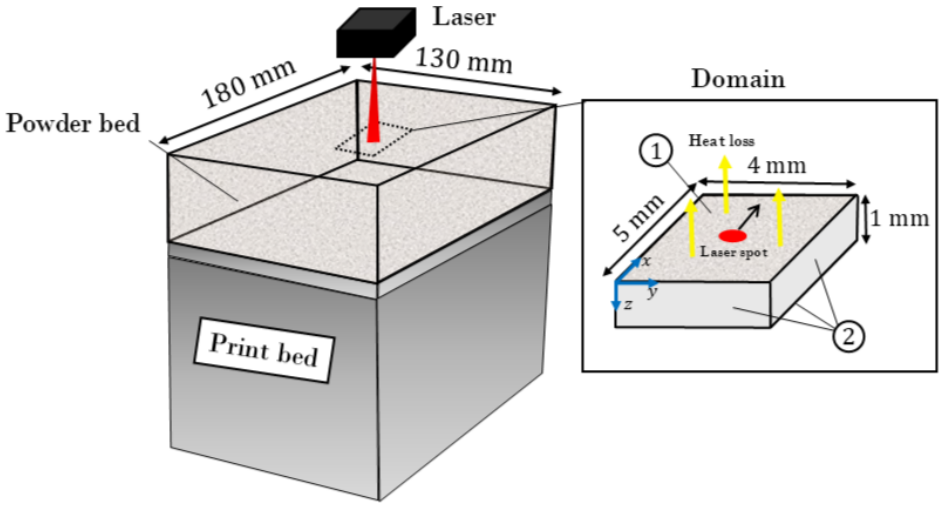

Figure 1: Illustration of Domain (Adapted from [6])

Since the model is at the micro-scale, the simulated domain represents only a small section of the powder bed (see Figure 1), which measures $5\,\mathrm{mm} \times 4\,\mathrm{mm} \times 1\,\mathrm{mm}$.

Heat losses to the environment are assumed to occur only through the top surface of the domain. Hence, the first boundary condition on the powder bed surface, (1) in Figure 1, includes both radiation and convection effects:

$$\dot{q}_{top} = -\vec{n}_{top} \cdot (k\nabla T) = -h\,(T - T_\infty) - \sigma_B \varepsilon \left(T^4 - T_\infty^4\right) \tag{3}$$

In (3), $\vec{n}_{top}$ is the normal vector to the top surface, h is the natural convection coefficient $[\mathrm{W/m^2K}]$, T_∞ is the ambient temperature $[\mathrm{K}]$, σ_B is the Stefan–Boltzmann constant $[\mathrm{W/m^2K^4}]$, and ε is the surface emissivity.

For the remaining boundaries, (2) in Figure 1, the heat from the laser is assumed to have no effect, as the laser is far from them. As a result, the temperature on both sides of these boundaries is considered equal. Therefore, an insulation boundary condition is applied:

$$\dot{q}_{rem} = -\vec{n}_{rem} \cdot (k\nabla T) = 0 \tag{4}$$

In (4), $\vec{n}_{rem}$ represents the normal direction at the remaining boundaries.

2.1.2. Phase Transformation

This subsection focuses on modeling the properties associated with the phase change, a highly nonlinear thermal process involving the melting and solidification of the material.

Specific Heat Capacity Due to the highly nonlinear nature of the phase transformation, data from Differential Scanning Calorimetry (DSC) at a prescribed heating rate of $10\,\mathrm{K/min}$ was utilized from [7]. The data is presented in Figure 2.

From the data, the temperature dependent specific heat capacity can be obtained using the relation between heat flux and specific heat [8]:

$$\dot{Q}(T) = m \cdot c_p^s(T) \cdot \dot{T} \tag{5}$$

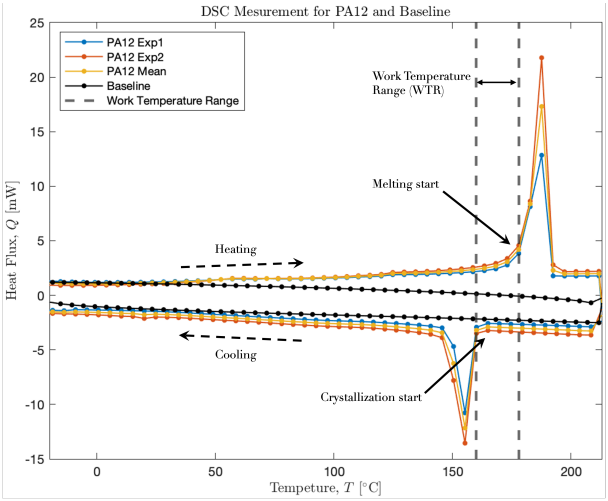

Figure 2: $\dot{Q}$-T curve for PA12 from DSC experiment. Taken from [7]

For which a piecewise function fit through the data was performed. The function fit from [7] can be seen in Figure 3.

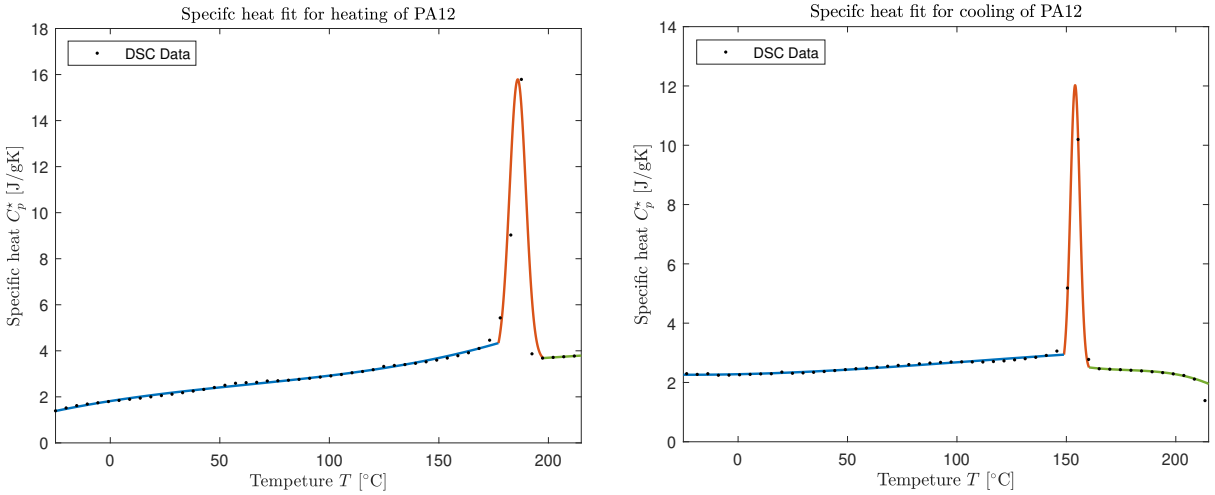

(a) Function fit for heating data of specific heat from DSC

(b) Function fit for cooling data of specific heat from DSC

Figure 3: Piecewise fit of DSC data for specific heat. Taken from [7]

From [7], the following function is obtained for the heating data:

$$C_{p,H}^{\star}(T) = \begin{cases} 4.5 \cdot 10^{-7} \cdot T^3 - 8.4 \cdot 10^{-5} \cdot T^2 + 0.02 \cdot T + 1.8, & T < 177.2\,^{\circ}\mathrm{C} \\ 3.6 + \frac{70}{\sqrt{\pi \cdot \left(\frac{42}{4}\right)}} \cdot \exp\left(-\frac{4 \cdot (T-186)^2}{\left(\frac{42}{4}\right)^2}\right), & 177.2\,^{\circ}\mathrm{C} \leq T < 197.7\,^{\circ}\mathrm{C} \\ -6.26 \cdot 10^{-6} \cdot T^2 + 0.0088 \cdot T + 2.19, & T \geq 197.7\,^{\circ}\mathrm{C} \end{cases} \tag{6}$$

For the cooling data, the following expression is obtained from [7]:

$$C^{\star}_{p,C}(T) = \begin{cases} -6.7 \cdot 10^{-6} \cdot T^3 + 0.0036 \cdot T^2 - 0.64 \cdot T + 40.7, & T < 149\,^{\circ}\mathrm{C} \\ 2.4 + \frac{29.54}{\sqrt{\pi \cdot 3}} \cdot \exp\left(-\frac{(T-154)^2}{3^2}\right), & 149\,^{\circ}\mathrm{C} \leq T < 160\,^{\circ}\mathrm{C} \\ -1.1 \cdot 10^{-7} \cdot T^3 + 3.4 \cdot 10^{-5} \cdot T^2 + 0.002 \cdot T + 2.3, & T \geq 160\,^{\circ}\mathrm{C} \end{cases} \tag{7}$$

To switch between the heating and cooling case, a switch variable, HorC, is introduced, where HorC $= 1$ if the material is being heated, and HorC $= 0$ if the material is being cooled. How the switch variable is defined will be further elaborated in subsubsection 2.2.2

$$C^{\star}_{p}(T) = \text{HorC} \cdot C^{\star}_{p,H}(T) + (1 - \text{HorC}) \cdot C^{\star}_{p,C}(T) \tag{8}$$

Thus, by utilizing data from DSC, a function describing the nonlinear behavior of the phase transformation for the temperature-dependent specific heat is obtained. However, it is also necessary to model the density, as it changes in nonlinear ways during the phase transformation. Density Change To describe the densification, it is essential to understand the underlying sintering mechanism. In this model, viscous sintering is assumed, where a noncrystalline material reduces its surface free energy by minimizing its surface area, leading to the merging of particles [9]. For noncrystalline materials, the densification process can be modeled based on the viscosity of the material. This is represented by the following differential equation [10]:

$$\frac{\mathrm{d}\rho}{\mathrm{d}t} = (\rho_{\text{solid}} - \rho)\,\eta_0 \exp\left(-\frac{E_a}{RT}\right) \tag{9}$$

In (9), the term $\eta_0 \exp\left(-\frac{E_a}{RT}\right)$ describes the rate at which the viscosity of the powder decreases with increasing temperature, T, thus enhancing the viscous sintering process. Here, η_0 is a pre-exponential factor $[1/\mathrm{s}]$, E_a is the activation energy $[\mathrm{J/mol}]$, and R is the universal gas constant $[\mathrm{J/molK}]$. The term $(\rho_{\text{solid}} - \rho)$ represents how particles have less room to move as they merge, which in turn slows down the densification. In this context, ρ_{solid} is the density of the solid material, and ρ is the local density of the material.

It should be noted, however, that (9) is only valid for non-crystalline polymers. Since the polymer described in this model is semi-crystalline, a correction term is needed to account for the retardation caused by crystallinity [11]. This leads to the modified equation:

$$\frac{\mathrm{d}\rho}{\mathrm{d}t} = (\rho_{\text{solid}} - \rho)\,\eta_0 \exp\left(-\frac{E_a}{RT} - \beta\chi\right) \tag{10}$$

In (10), β is an empirically determined crystalline coefficient, and χ denotes the crystallinity fraction, where $\chi = 1$ represents the initial crystallinity of the powder, and $\chi = 0$ indicates a non-crystalline state.

The crystalline fraction is described using eq.(6), and based on the assumption that PA12 is non-crystalline at its melting point T_m and exhibits its full initial crystalline at the print bed temperature T_0. During the heating process, the crystalline fraction, $\chi(T_{\text{max}})$, decreases from 1 to 0 as the temperature approaches T_m, after which it remains constant at 0:

$$\chi(T_{\text{max}}) = \begin{cases} \frac{C^{\star}_p(T_{\text{max}}) - C^{\star}_p(T_m)}{C^{\star}_p(T_0) - C^{\star}_p(T_m)}, & \text{if } T_0 \leq T_{\text{max}} \leq T_m \\ 0, & \text{if } T_{\text{max}} > T_m \end{cases} \tag{11}$$

Once the laser heating ceases, the print bed temperature remains above the recrystallization point, preventing the crystalline fraction from reaching the recrystallization temperature, as shown in Figure 3. Thus, the material does not recrystallize and retains the crystallinity fraction it achieved during heating. Therefore, the crystalline fraction depends on the maximum temperature each particle experiences during sintering. The definition of the maximum

temperature will be elaborated in subsubsection 2.2.2.

Thermal Conductivity During the phase transformation, the powder material is bonded into a solid structure, effectively eliminating the air-filled voids between particles. This results in a significant change in thermal conductivity. The thermal conductivity of the powder can be expressed as a function of its porosity, ϕ, as described in [12]:

$$k_{\text{powder}} = k_{\text{solid}}(1 - \phi) \tag{12}$$

where k_{solid} is the thermal conductivity of the material at full density, ρ_{solid}. In this equation, it is assumed that the contribution of air to the thermal conductivity, k_{air}, is negligible, as still air between the powder particles acts as an excellent insulator.

According to [3], the porosity ϕ, can be described as the fraction between the current density, ρ and the material at full density ρ_{solid}:

$$\phi(\rho) = \frac{\rho_{\text{solid}} - \rho}{\rho_{\text{solid}}} \tag{13}$$

The porosity varies from the initial value, ϕ_{initial}, of the powder bed to $\phi_{\text{min}} = 0$ when the material is fully densified.

2.1.3. Laser Beam Model

SLS printers utilize a high-powered CO_2 laser beam as a thermal energy source to fuse powder particles together. According to [3, 12], the intensity of the laser beam, $[\mathrm{W}/\mathrm{m}^2]$, follows a Gaussian distribution across the radius of the beam:

$$\dot{q}_s(x, y) = K \cdot n \cdot \frac{P_{\text{laser}}}{\pi R_{\text{laser}}^2} \cdot \exp\left(-n \frac{(x - x_c)^2 + (y - y_c)^2}{R_{\text{laser}}^2}\right) \tag{14}$$

where K is an absorption coefficient, describing the material's heat absorption; n is a Gaussian shape factor, which controls the concentration of laser rays, with a higher n indicating a more concentrated distribution of rays at the beam center. R_{laser} represents the radius of the laser beam, and P_{laser} is the laser power. The coordinates x_c and y_c define the position of the laser beam's center.

To simulate the laser beam's movement along a straight line, the y-coordinate of the laser center is set to a constant value, $y_c = y_0$, while the x-coordinate follows:

$$x_c = V_x \cdot t + x_0 \tag{15}$$

Here, V_x is the laser scanning speed, and x_0 is the initial x-position of the laser.

In addition to modeling the laser's distribution across the surface, as described in eq. (14), it is also necessary to account for the transmission of the laser through the powder. According to [12] the laser absorption and diffusion in the powder follows Beer-Lambert's law:

$$\frac{\partial}{\partial z}\dot{q}_V(x, y, z) = -\dot{q}_V(x, y, z)\gamma^{-1} \tag{16}$$

Here, γ is the attenuation length, which is defined in [13] as; *the depth into the material along the direction of the radiation at which the intensity of the radiation falls to $\frac{1}{e}$ of its value at the surface*. In this context, e represents Euler's number, indicating that approximately 63% of the laser light photons are absorbed within this depth.

Solving eq. (16) as an initial value problem with the initial condition $\dot{q}_V(x, y, 0) = \dot{q}_s(x, y)$ from eq. (14), the

solution for the heat source in 3D is given by:

$$\dot{q}_V(x, y, z) = \dot{q}_s(x, y)\gamma^{-1} \exp\left(-z\gamma^{-1}\right) \tag{17}$$

With the interaction between the laser beam and the powder bed described, the necessary theoretical framework for modeling heat transfer during the SLS process at the micro-scale has been established. The next step is to implement this theory and model into finite element (FE) software for simulation.

2.2. Method

This section outlines the methods employed to effectively implement the theoretical framework into the FE software COMSOL Multiphysics. The process involves translating the established theoretical model into a computational environment, ensuring accurate representation of the underlying physics and enabling efficient simulation of the SLS process.

2.2.1. Boundary Condition Implementation

Accurate implementation of boundary conditions is crucial to ensuring that a simulation reflects the physical constraints of the system being modeled.

As illustrated in Figure 1, the boundaries, labeled (2), are assumed to be far enough from the laser such that no significant temperature gradient exists across these regions. To enforce this assumption in the simulation, the center of the laser beam in the x-direction is constrained to maintain a minimum distance of $x_{0,\text{min}} = \frac{L_x}{4}$ from the boundary, where L_x represents the length of the computational domain in the x-direction. This condition is implemented numerically using an on/off switch, x_{switch}, which is multiplied to eq. (17), and defined by the following Boolean logic.

$$x_{\text{switch}} = \begin{cases} 1 & \text{if } x_{\text{c}} < \frac{L_x}{4} \\ 0 & \text{otherwise} \end{cases} \tag{18}$$

Thus, when x_c approaches the boundary, x_{switch} becomes zero, deactivating the Gaussian heat source term. In the y-direction, the laser center is positioned at the center of the domain.

To enhance computational efficiency, the symmetry around the center of the Gaussian heat distribution is exploited. The simulated domain is halved along the x-direction, at the location of the laser beam's center in the y-direction. This allows the application of a symmetric boundary conditions, significantly reducing the computational cost of the simulation.

2.2.2. State Variables and Phase Transitions

This section describes the methodology for tracking the phase transition using state variables in COMSOL Multiphysics. Monitoring the phase transition requires maintaining a record of the maximum temperature at specific points in the spatial domain.

To achieve this, a state variable T_{Max} is defined. The state variable uses Gauss points within each element, to store the temperature data. To store the peak temperature recorded at Gauss points during the simulation. Initially, T_{Max} is set to the initial temperature at each point within the domain. The variable is subsequently updated at each time step for all points according to the following criteria:

$$T_{\text{Max}} = \begin{cases} T & \text{if } T > T_{\text{Max}}, \\ T_{\text{Max}} & \text{otherwise.} \end{cases}$$

This expression compares the current temperature T with the value stored in T_{Max}. If the current temperature exceeds T_{Max}, the latter is updated to reflect the new temperature. Otherwise, T_{Max} remains unchanged. This approach ensures that T_{Max} at each Gauss point always holds the highest temperature encountered during the simulation. Note: The values at these Gauss points are extrapolated and interpolated over the entire element, which may result in slight differences compared to the temperature field stored at the nodal points [14].

Using the maximum temperature, a state variable, HorC, is introduced to determine whether a point should follow the heating or cooling curve of the specific heat capacity function, described in eq. (7) and (6). Initially, HorC is set to 1, indicating that the heating curve (eq. (6)) should be followed (see eq. (8)). The variable updates according to the following logic:

$$\text{HorC} = \begin{cases} 1, & \text{if } T > T_{\text{Max}}, \\ 0, & \text{if } T < T_{\text{Max}} \text{ and } T > T_{\text{ms}}, \\ 1, & \text{if } T < T_{\text{sf}}, \\ \text{HorC}, & \text{otherwise.} \end{cases} \tag{19}$$

The expression checks whether the current temperature T is below the maximum temperature T_{Max}. If this condition is satisfied, and T exceeds the temperature at which melting starts T_{ms}, the point follows the cooling curve (Eq. (7)), to prevent the release of latent heat before reaching the crystallization temperature T_s. Once the temperature drops below the crystallization endpoint T_{sf}, all latent heat has been released, and the point transitions to following the heating curve (Eq. (6)). Should the temperature rise above the maximum temperature T_{Max}, the point will follow the heating curve, thereby absorbing more latent heat.

Note: Ideally, T_{Max} should be reset once the temperature drops below the crystallization endpoint. However, in this specific simulation, the powder is not expected to be reheated beyond T_{sf}, making this reset unnecessary and therefore not implemented.

2.2.3. Mesh Generation and Optimization

This section describes the process of generating an optimized mesh to ensure precise and efficient numerical results. Given the rectangular nature of the domain, hexahedral elements are utilized as they are well-suited for meshing rectangular geometries.

To minimize computational time, the mesh is coarser in areas distant from the heat source and becomes increasingly refined in the scanned region. This region is square in both the width and depth directions of the heat source. The heat source is discretized into 128 elements (16×16) in the plane, with 8 elements in the depth direction of the scanned region to accurately capture thermal gradients. Figure 4 shows a diagonal line that divides the boundary into two symmetrical sections, mapped using a predefined distribution with a linear growth rate (number of elements: 7, element ratio: 5). This strategy allows for gradual refinement of the mesh towards the scanned region. The remainder of the domain is swept with hexahedral elements, maintaining a maximum element size of 0.05mm to ensure sufficient resolution throughout the geometry.

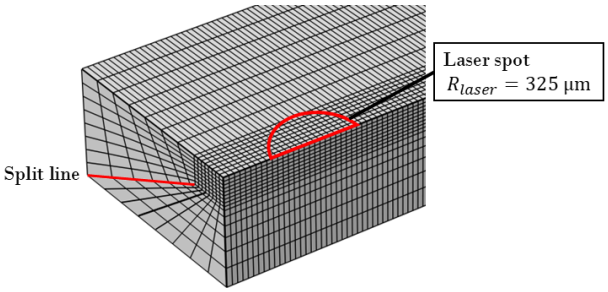

Figure 4: Illustration of the mesh

2.2.4. Solver Configuration and Convergence

In this simulation, the laser heat source is represented as a Gaussian wave traveling across the discretized grid of the domain. According to [15], to compute the amplitude of the wave at discrete time steps, the distance traveled by the wave during a time step must be less than the distance to adjacent grid points. This ensures that information from a given mesh element propagates only to its immediate neighbors.

Since the laser moves in a single direction, the one-dimensional form of the Courant-Friedrichs-Lewy (CFL) condition can be applied, expressed as [15]:

$$C = V_x \cdot \frac{\Delta t}{\Delta x} \tag{20}$$

where Δt denotes the time step $[\mathrm{s}]$, V_x is the velocity of the laser $[\mathrm{m/s}]$, and Δx represents the spacing between adjacent grid points $[\mathrm{m}]$. For explicit time solvers, the Courant number C must typically remain at or below, $C_{\text{max}} = 1$ [15].

If the ratio of mesh size, velocity, and time step exceeds this limit ($C > 1$), numerical instability may arise. To satisfy the CFL condition given in (20), the maximum allowed time step when the laser is in motion is constrained by:

$$\Delta t = \frac{L_x}{V_x \cdot N_{ele}} \tag{21}$$

where L_x is the length of the meshed domain in the scanning direction $[\mathrm{m}]$, and N_{ele} represents the number of mesh elements in this direction. It is worth noting that the CFL condition is only critical during the laser's movement. During the subsequent cooling phase, the time step can be significantly increased to optimize computational efficiency:

$$\Delta t = \frac{t_{\text{end}}}{50} \tag{22}$$

In this expression, t_{end} denotes the total duration of the simulation.

2.2.5. Parameters

The method described in the previous subsections was used to simulate the printing process in a Sinterit Lisa X SLS 3D printer. The simulated printing material is industrial PA-12, as it is one of the most commonly used materials for SLS 3D printing [4]. All the parameters used are listed in Table 1 below.

Property	Value	Unit (Symbol)	Source
Absorption coefficient, K	0.4	$[-]$	[12]
Activation energy, E_A	102	$[\mathrm{kJ/mol}]$	[7]
Ambient temperature T_∞	140	$[^\circ\mathrm{C}]$	Sinterit Studio
Avg. Laser Power, P_{laser}	7.85	$[\mathrm{W}]$	Sinterit Studio
Avg. Laser Scanning Speed, V_x	1.1	$[\mathrm{m/s}]$	Sinterit Studio
Bulk density, ρ_{bulk}	505	$[\mathrm{kg/m^3}]$	[16]
Convection coefficient, h	15	$[\mathrm{W/(m^2{\cdot}K)}]$	[12]
Crystalline coefficient, β	10	$[-]$	[7]
Density of solid material, ρ_{solid}	1030	$[\mathrm{kg/m^3}]$	[16]
Domain length, L_x	5	$[\mathrm{mm}]$	$[-]$
Domain thickness, L_z	1	$[\mathrm{mm}]$	$[-]$
Domain width, L_y	4	$[\mathrm{mm}]$	$[-]$
Attenuation length, γ	$1.11 \cdot 10^4$	$[\mathrm{m}]$	[12]
Initial temperature, T_0	175	$[^\circ\mathrm{C}]$	[7]
Laser Radius, R_{laser}	0.325	$[\mathrm{mm}]$	[17]
Melting point, T_m	186.2	$[^\circ\mathrm{C}]$	Figure 3
Rate of structural change, η_0	$5 \cdot 10^{13}$	$[\mathrm{s^{-1}}]$	[7]
Surface emissivity, ϵ	0.8	$[-]$	[12]
Thermal conductivity of solid, k_{solid}	0.23	$[\mathrm{W/(m \cdot K}]$	[16]

Table 1: Summary of parameters used in micro scale simulation.

3. Part Scale Modeling

This chapter focuses on the theoretical framework and approach for simulating the heat transfer mechanisms at the part scale.

3.1. Theory

To model the SLS process at the part scale, it is essential to consider the following factors:

1. Addition of new layers in a continually meaner.
2. Heat transfer mechanisms within the powder and solid material.
3. Interactions between the laser beam and the powder bed.
4. Phase transformation from powder to solid during the sintering process.
5. The duty cycle of the laser.

3.1.1. Addition of Layers

In the SLS process, new layers of powder are deposited over previously sintered ones and selectively fused by a laser, resulting in the part growing incrementally over time [4]. In numerical simulations, this layer-by-layer nature is often modeled using flash heating (FH) methods, where elements are progressively activated to represent the addition of new layers [2].

While effective, defining the elements for each layer in the FH method can be a complex process. To address this challenge, a continuous modeling approach is proposed. Instead of individually activating and heating each layer, the entire geometry, including all layers, is modeled as a single entity. Inactive layers are represented by modifying their thermal conductivity, k, to an extremely low value, effectively simulating their absence and preventing heat transfer between active and inactive layers.

This behavior is governed by a step function, as illustrated in Figure 5, which moves upward with the heat source. The step function is mathematically described as:

$$\text{step}(z) = 1 - \left(\frac{1}{2} \cdot \left(1 + \tanh \left(\frac{z - z_c}{\frac{h_{\text{layer}}}{6}} \right) \right) \cdot \left(1 - 10^{-16} \right) \right) \tag{23}$$

Here, z_c represents the center of the step function, which varies over time to simulate the addition of new layers:

$$z_c = v_z \cdot t + z_0 \tag{24}$$

where v_z is the vertical velocity of the printer, and z_0 is the initial height of the printing process.

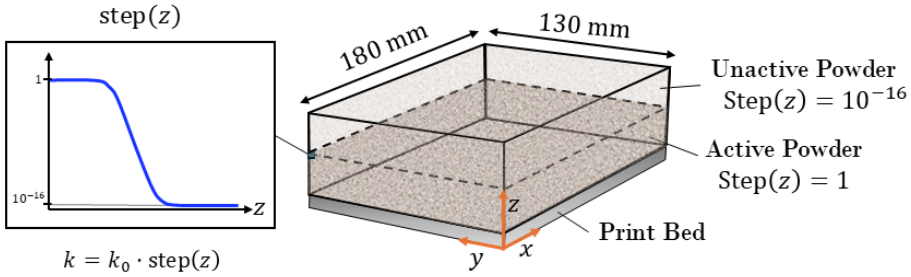

Figure 5: Illustration of layer addition.

3.1.2. Heat Transfer Equation

The heat transfer mechanisms during the SLS process at the part scale can be described by the heat conduction equation [5]:

$$\rho C_p^{\star} \frac{\partial T}{\partial t} + \nabla \cdot (-k \nabla T) = \dot{q}_V + \dot{q}_{\text{conv},V} + \dot{q}_{\text{rad},V} \tag{25}$$

In (25), ρ is the material density $[\text{kg/m}^3]$, $C_p^{\star}$ is the specific heat capacity of the material $[\text{J}/(\text{kg} \cdot \text{K})]$, k is the thermal conductivity $[\text{W}/(\text{m} \cdot \text{K})]$, and $\dot{q}_V$ represents the volumetric thermal input from the laser $[\text{W/m}^3]$.

The terms $\dot{q}_{\text{conv},V}$ and $\dot{q}_{\text{rad},V}$ account for heat losses due to convection and radiation, during the SLS process. These terms are included to account for the continuous nature of the simulation. During the SLS printing process, the top boundary of each layer is exposed to the environment, leading to heat losses. However, in the simulation, the boundaries of the domain remain fixed, which prevents the use of traditional convection and radiation boundary conditions. This limitation and the treatment of heat losses will be elaborated further in the following section.

Initial and Boundary Conditions In the SLS process, the top of the powder bed is heated to the processing temperature, T_0, using an IR heater before exposure to the laser. It is then maintained at T_{side} during processing by piston and cylinder heaters [18] (see Figure 6). Thus, it is assumed that the temperature of the newly added layer is uniform throughout. The initial condition is therefore defined as:

$$T(x, y, z, 0) = T_0 \tag{26}$$

As mentioned, radiation and convection heat losses from the top surface are modeled as moving heat sinks due to the addition of new layers. In the simulation, these losses are accounted for by subtracting their contributions from the heat source. This approach effectively removes the heat that would otherwise be lost to radiation and convection before it enters the system. The intensity of the convection heat loss is defined as:

$$\dot{q}_{\text{conv}} = h_{\text{air}}(T_{\text{air}} - T) \tag{27}$$

where h_{air} is the convection heat transfer coefficient of air, T is the surface temperature, and T_{air} is the surrounding air temperature, assumed to be equal to the initial temperature at the top of the powder bed, $T_{\text{air}} = T_0$.

Similarly, the heat loss intensity due to radiation is given by:

$$\dot{q}_{\text{rad}} = \epsilon \sigma_B \left(T_{\text{air}}^4 - T^4 \right) \tag{28}$$

where ϵ is the emissivity, and σ_B is the Stefan–Boltzmann constant. The temperatures T and T_{air} are the same as those used in the convection heat transfer equation. The implementation of $\dot{q}_{\text{conv}}$ and $\dot{q}_{\text{rad}}$ as a heat sink will be further detailed in subsubsection 3.1.3.

As shown in Figure 6, the temperature during the processing phase is maintained at a constant temperature T_{side} by piston and cylinder heaters.

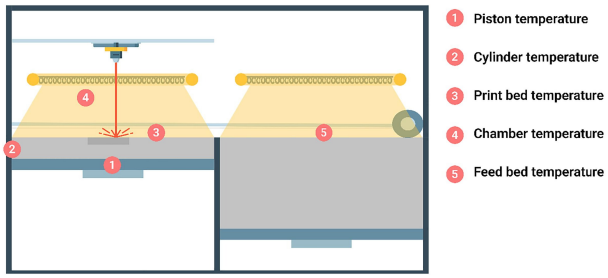

Figure 6: Schematic of temperature control in the Sinterit Lisa SLS 3D printer. Taken from [18]

The heat flux through the piston and cylinder boundary is modeled using a convection heat transfer approach, inspired by the method in [19]:

$$\dot{q}_{\text{side}} = -\vec{n}_{\text{side}} \cdot (k \nabla T) = -h_{\text{side}} \left(T - T_{\text{side}} \right) \tag{29}$$

In (29), $\vec{n}_{\text{side}}$ is the normal vector to the piston and cylinder surfaces, h_{side} is the equivalent convection coefficient corresponding to the heat transfer between these surfaces, and T_{side} is the temperature maintained by the piston and cylinder heaters.

Once the part is fully printed, the cooling stage begins, during which the powder bed cools to room temperature. At this stage, radiation and convective heat losses to the environment are assumed to occur on the top surface of the domain. The boundary condition for the cooling stage is given by:

$$\dot{q}_{\text{top, cool}} = -\vec{n}_{\text{top}} \cdot (k \nabla T) = -h_{\text{air}} \left(T - T_{\text{room}} \right) - \sigma_B \varepsilon \left(T^4 - T_{\text{room}}^4 \right) \tag{30}$$

In (30), $\vec{n}_{\text{top}}$ is the normal vector to the top surface, and T_{room} is the room temperature $[\text{K}]$.

For the piston and cylinder boundaries during the cooling stage, it is assumed that the heaters are turned off. Therefore, at the time of cooling, it is assumed in eq. (29) that:

$$T_{\text{side}} = T_{\text{room}} \tag{31}$$

3.1.3. Laser Source Model

Before defining the laser source model, the volumetric energy density should be considered. The volumetric energy density describes the amount of energy supplied by the laser to the material per unit volume. During the printing process, the laser aims to maintain this energy density constant to ensure consistent material processing.

It is defined in [4]:

$$E_v = \frac{P_0}{v_{\text{laser}} \cdot h_{\text{hatch}} \cdot h_{\text{layer}}} \tag{32}$$

Where P_0 is the laser power $[\mathrm{W}]$, v_{laser} is the scanning speed of the laser $[\mathrm{m/s}]$, h_{hatch} is the hatch spacing $[\mathrm{m}]$, and h_{layer} is the layer thickness $[\mathrm{m}]$. The fraction of this energy absorbed in the material, is described by the absorption coefficient, K [20]. To take this into account, a modified version of the energy density is defined as

$$E_v^* = \frac{K \cdot P_0}{v_{\text{laser}} \cdot h_{\text{hatch}} \cdot h_{\text{layer}}} \tag{33}$$

It is essential that the laser is modeled such that the heat transferred to the powder over time equals the desired energy density. It is important to note that the heat transfer is not constant over time, and therefore the energy density should be equal to the heat transferred by the laser, integrated over time:

$$E_v^\star = \int_{-\infty}^{\infty} \dot{q}_V(z,t)\, dt \tag{34}$$

It is beneficial to define $\dot{q}_V(z,t)$ as the product of two components:

$$\dot{q}_V(z,t) = \dot{q}_0 \cdot f(z,t) \tag{35}$$

Where $f(z,t)$ is a Gaussian function defined such that the integral of the function over z is equal to one:

$$\int_{-\infty}^{\infty} f(z,t)\, dz = 1 \tag{36}$$

This results in the Gaussian function being expressed as:

$$f(z,t) = \frac{1}{\sigma\sqrt{2\pi}} \exp\left(-\frac{1}{2}\left(\frac{z - v_z t}{\sigma}\right)^2\right) \tag{37}$$

Here, σ represents the standard deviation of the Gaussian distribution. Eq. (37) describes the distribution of the laser power in the vertical direction over time, with the center of the Gaussian profile moving upwards with the vertical velocity of the printer, v_z.

To determine the heat source intensity $\dot{q}_0$, eq. (35) is inserted into eq. (34), noting that $\dot{q}_0$ is independent of time. The integral evaluates to:

$$E_v^\star = \dot{q}_0 \cdot \int_{-\infty}^{\infty} f(z,t)\, dt = \frac{\dot{q}_0}{v_z} \tag{38}$$

Thus, by inserting the definition of the energy density from eq. (33), $\dot{q}_0$ becomes:

$$\dot{q}_0 = \frac{P_0 \cdot K \cdot v_z}{v_{\text{laser}} \cdot h_{\text{hatch}} \cdot h_{\text{layer}}} \tag{39}$$

The heat sinks described in subsubsection 3.1.2 account for the convection and radiation heat losses at the top surface. These are defined similarly to eq. (35):

$$\dot{q}_{\text{conv},V} = \dot{q}_{\text{conv}} \cdot f(z,t) \quad \text{and} \quad \dot{q}_{\text{rad},V} = \dot{q}_{\text{rad}} \cdot f(z,t) \tag{40}$$

Where the convection, $\dot{q}_{\text{conv}}$, and radiation, $\dot{q}_{\text{rad}}$, intensities are defined in eq. (27) and (28), respectively. $f(z,t)$ is the Gaussian function described in eq. (36).

Thus, the laser has been implemented as a heat source, while the radiation and convective heat losses at the top of the powder bed surface are added as heat sinks.

3.1.4. Phase Transformation

Phase changes are not always easy to model, especially when hysteresis has to be considered. When a phase change occurs, latent heat is either absorbed or released, and with hysteresis, this happens at different temperatures, depending on whether the material is melting or solidifying. Furthermore, parameters like density, which is typically assumed to have a constant value, change rapidly.

Specific Heat Capacity As shown in Figure 2, PA12 is a phase-change material with hysteresis, where the solidification temperature differs from the melting temperature. The part-scale model incorporates this behavior using a hysteresis model inspired by [21], illustrated schematically in Figure 7.

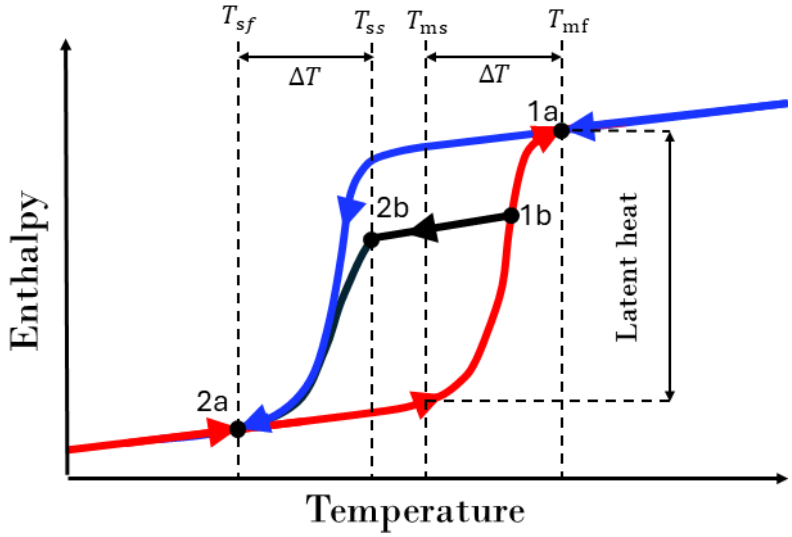

Figure 7: Schematic of hysteresis model.

The phase changes are described using a step function for both melting and solidification:

$$s(T) = \frac{1}{2}\left(1 + \tanh\left(\frac{T}{\frac{\Delta T}{8}}\right)\right), \tag{41}$$

where $\Delta T = 20.5\text{K}$ is the width of the phase transformation, determined based on Figure 2.

In Figure 7, heating the material from the solid powder state follows the lower red path, defined by:

$$h_{\text{heating}}(T) = C_{p,0}T + L_h \cdot s(T - T_m), \tag{42}$$

where L_h is the specific latent heat $[\text{J/kg}]$, T_m is the melting temperature $[\text{K}]$, and $C_{p,0}$ is the mean baseline specific heat capacity when the material is not undergoing a phase change $[\text{J}/(\text{kg} \cdot \text{K})]$.

When fully melted (point 1a), the material transitions to the liquid phase. Upon cooling, the material follows the

upper blue path, remaining in the liquid phase below the melting temperature. This path is given by:

$$h_{\text{cooling}}(T) = C_{p,0}T + L_h \cdot s(T_{\max} - T_m) \cdot s(T - T_s), \tag{43}$$

where T_s is the solidification temperature [K], and $T_{\max}$ is the maximum temperature reached, as defined in subsubsection 2.2.2.

Once solidification completes (point 2a), the material reverts to the red path. For cases involving partial melting and subsequent cooling, such as point 1b, the material follows the black path between the red and blue curves. Here, $s(T_{\max} - T_m)$ in eq.(43) adjusts the latent heat released based on the latent heat absorbed. For example, if 50% of the latent heat is absorbed during heating, $s(T_{\max} - T_m) = 0.5$, releasing only 50% of the latent heat during cooling.

The specific heat capacity, accounting for the hysteresis behavior, is expressed as:

$$C_p^{\star}(T) = \text{HorC} \cdot \frac{\mathrm{d}}{\mathrm{d}T} h_{\text{heating}}(T) + (1 - \text{HorC}) \cdot \frac{\mathrm{d}}{\mathrm{d}T} h_{\text{cooling}}(T), \tag{44}$$

where HorC is a state variable, defined in subsubsection 2.2.2, that determines whether a point follows the heating or cooling curve.

Density As the powder undergoes sintering, transforming from a porous powder to a solid mass, the density changes, which must be accounted for in the model. Before sintering, the density of the powder is ρ_{bulk}, and after complete sintering, the density becomes ρ_{solid}. This transition is modeled using a step function that adjusts the density based on the maximum temperature experienced by a given volume of the print:

$$\rho(T_{\max}) = \rho_{\text{bulk}} + \frac{\rho_{\text{solid}} - \rho_{\text{bulk}}}{2} \cdot \left(1 + \tanh\left(\frac{T_{\max} - T_m}{\frac{\Delta T}{8}}\right)\right), \tag{45}$$

where $T_{\max}$ represents the highest temperature reached in the volume, defined in subsubsection 2.2.2.

Using $T_{\max}$ ensures that the density does not change after sintering, even as the part cools, preventing the density from reverting to ρ_{bulk}, which would occur if the current temperature were used. Eq. (45) is centered around the powder's melting temperature, T_m. The transition zone width, $\Delta T = 20.5$ K, corresponds to the phase transformation width determined based on Figure 2.

The thermal conductivity is defined in the same manner as in the micro-scale model (Equation 2.1.2):

$$k_{\text{powder}}(\rho, z) = k_{\text{solid}}(1 - \phi(\rho)) \cdot \text{step}(z), \tag{46}$$

where $\phi(\rho)$ is the porosity defined in eq.(13), and step(z) is the step function from eq.(23), which determines whether a layer is active or not.

A potential issue with this density modeling approach is that when the density increases, so does the mass, and consequently, the energy. In reality, as the material density increases, the material shrinks, and the resulting gap is filled with unsintered powder once the next layer is added. The additional powder filling the shrinkage gap requires further energy for sintering. This energy must be supplied by the laser. However, in the model, this additional energy is not directly taken from the laser but instead appears as an energy increase unaccounted for by the laser's contribution. While this is physically impossible, the model is accepted, because the additional mass and energy correspond to the powder added to fill the cavity. This is indirectly accounted for when determining laser power based on the desired energy density, as described in subsubsection 3.1.3.

3.1.5. Duty Cycle

In the SLS process, the laser does not operate continuously. Instead, it alternates between being active and inactive. During each cycle, the laser selectively fuses regions of the powder layer, and a fresh layer of powder is spread before the next scan begins [4].

To account for this duty cycle, the activation time of the laser, t_{on}, is defined as the duration for which the laser is active in a given region, while the inactive time, t_{off}, is the duration for which the laser is not active. To relate the duty cycle to the build speed v_z, t_{off} is expressed as:

$$t_{\text{off}} = \frac{h_{\text{layer}}}{v_z} - t_{\text{on}}, \tag{47}$$

To adjust for the fact that the laser is not active continuously, a compensation factor, η_D, is introduced:

$$\eta_D = \frac{t_{\text{on}} + t_{\text{off}}}{t_{\text{on}}}. \tag{48}$$

This factor ensures that the total energy input remains consistent with a continuous operation. For instance, if $t_{\text{on}} = t_{\text{off}}$, the laser is active for half the time, resulting in $\eta_D = 2$. This effectively doubles the laser intensity to deliver the same energy as in the continuous case.

To represent the laser's state, a binary variable, ON_{OFF}, is defined, which will be detailed in subsubsection 3.2.2. The variable equals 1 when the laser is active during t_{on}, and 0 when the laser is inactive during t_{off}.

With these modifications, the heat intensity of the laser, previously defined in eq. (35), is updated to:

$$\dot{q}_0 = \text{ON}_{\text{OFF}} \cdot \eta_D \cdot \frac{P_0 \cdot K \cdot v_z}{v_{\text{laser}} \cdot h_{\text{hatch}} \cdot h_{\text{layer}}}, \tag{49}$$

These modifications allow accurate modeling of the laser's energy deposition under the duty cycle constraints.

3.2. Method

This section outlines the methods employed to effectively implement the theoretical framework into the FE software COMSOL Multiphysics.

3.2.1. Domain Representation and Meshing

This section details the implementation of the computational domain and mesh generation for accurate numerical simulation.

To simplify geometry handling, the identity mapping function in COMSOL Multiphysics, is utilized. Two geometries are defined: the first represents the print bed, where the theoretical framework outlined in subsection 3.1 is applied, and the second contains the powder bed and printed parts. The identity mapping function is used to define a variable, turn_{off}, which is assigned a value of 1 in regions containing printed parts and 0 elsewhere, using the second geometry. This variable is multiplied by the volumetric heat source term, eq. (35), ensuring that the laser is active only within the printed regions.

The computational domain (geometry 1) is simplified to a rectangular box, enabling the use of hexahedral elements, which are well-suited for such geometries. In regions influenced by the Gaussian laser heat source, the mesh element size is set to σ, corresponding to the standard deviation of the laser power distribution in eq. (37).

To account for the upward motion of the heat source with velocity v_z, the time step is restricted by the CFL

criterion described in subsubsection 2.2.4, ensuring numerical stability:

$$\Delta t = \frac{1}{2} \cdot \frac{L_z}{v_z \cdot N_{\text{ele}}}, \tag{50}$$

where L_z is the domain length in the z-direction, and N_{ele} is the number of elements along that axis.

3.2.2. Solver Configurations and Duty Cycle

To incorporate the duty cycle into the simulation, explicit events are utilized in COMSOL Multiphysics. A discrete state variable, ON_{OFF}, is initialized to 0, indicating the laser is off. An explicit event is then defined to activate the laser ($\text{ON}_{\text{OFF}} = 1$) at $t_i = 0$, with a period of one cycle $T = t_{\text{on}} + t_{\text{off}}$. A second explicit event deactivates the laser ($\text{ON}_{\text{OFF}} = 0$) at $t_i = t_{\text{on}}$, repeating with the same period, T. This ensures the laser remains active for t_{on} and inactive for t_{off} in each cycle.

To accurately capture the energy input during t_{on}, the time-dependent solver is configured with a relative tolerance of 1×10^{-5}. This ensures sufficiently small time steps during events, maintaining numerical stability and convergence.

3.2.3. Parameters

The method described in the previous subsections was used to simulate the printing process in a Sinterit Lisa X SLS 3D printer. The simulated printing material is industrial PA-12, as it is one of the most commonly used materials for SLS 3D printing [4]. All the parameters used are listed in Table 2 below.

Property	**Value**	**Unit (Symbol)**	**Source**
Absorption coefficient, K	1	$[-]$	$[-]$
Avg. Laser Power, P_0	7.85	$[\text{W}]$	Sinterit Studio
Avg. Laser Scanning Speed, v_{laser}	1.1	$[\text{m/s}]$	Sinterit Studio
Vertical print velocity, v_z	14	$[\text{mm/h}]$	[17]
Initial temperature, T_0	175	$[^\circ\text{C}]$	[7]
Emissivity, ϵ	0.8	$[-]$	[12]
Convection coefficient of sides, h_{side}	10	$[\text{W}/(\text{m}^2 \cdot \text{K})]$	[19]
Specific heat capacity outside phase change, $C_{p,0}$	2	$[\text{kJ}/(\text{kg} \cdot \text{K})$	Figure 3
Convection coefficient top, h_{air}	15	$[\text{W}/(\text{m}^2 \cdot \text{K})]$	[12]
Latent heat, L_h	145	$[\text{kJ/kg}]$	Figure 3
Bulk density, ρ_{bulk}	505	$[\text{kg/m}^3]$	[16]
Density of solid material, ρ_{solid}	1030	$[\text{kg/m}^3]$	[16]
Temperature of melting start, T_{ms}	176	$[^\circ\text{C}]$	Figure 3
Temperature of solidification finished, T_{sf}	145	$[^\circ\text{C}]$	Figure 3
Melting temperature, T_m	186.2	$[^\circ\text{C}]$	Figure 3
Solidification temperature, T_s	155.3	$[^\circ\text{C}]$	Figure 3
Volumetric energy density, $E_v^\star$	1.59	$[\text{J/m}^3]$	Sinterit Studio
Hatch spacing, h_{hatch}	0.36	$[\text{mm}]$	Sinterit Studio
Layer height, h_{layer}	$n_{\text{layer}} \cdot 0.125$	$[\text{mm}]$	Sinterit Studio
Standard deviation of the Gaussian distribution, σ	$h_{\text{layer}}/3$	$[\text{mm}]$	$[-]$
Temperature of print bed, T_{bed}	170	$[^\circ\text{C}]$	Sinterit Studio

Table 2: Summary of parameters used in the part scale simulation.

4. Analysis & Discussion

In this chapter, the results from the micro- and part-scale models introduced in the previous chapters are presented and analyzed. The part-scale model from section 3 is primarily examined using 2D simulations to reduce com-

putational time, with a complementary 3D simulation included to capture additional complexities. Furthermore, a parameter study is conducted to investigate the influence of selected key parameters.

4.1. Presentation of Results

The theory and method presented in section 2 and 3, results in temperatures and densities that will be presented in this section. For the part scale, only 2D results are presented in this section.

4.1.1. Micro-Scale

For the micro-scale model described in section 2, the temperature and density results are presented in Figure 8 and Figure 9, respectively.

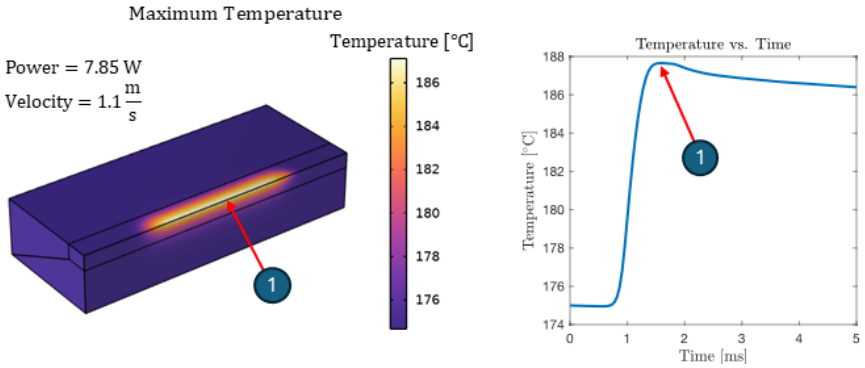

Figure 8: Temperature distribution and temporal evolution for the micro-scale model.

The left plot in Figure 8 shows the maximum surface temperature of the micro-scale model at $t = 0.1\,\mathrm{s}$, which is the end of the micro-scale simulation. Point 1, marked on this plot, corresponds to a specific location for which the temperature evolution over time is displayed in the right plot. The results indicate that the peak surface temperature reaches $T = 187.7°\mathrm{C}$, occurring within a rapid heating period of approximately $t = 1\,\mathrm{ms}$. The subsequent cooling phase is not included in the figure due to its significantly larger time scale.

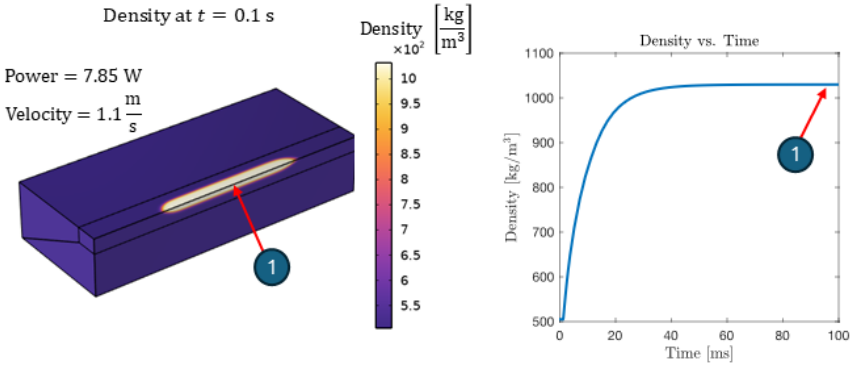

Figure 9: Density distribution and temporal evolution for the micro-scale model.

In Figure 9, the left plot displays the density distribution on the model's surface at $t = 0.1\,\mathrm{s}$. High-density regions correspond to sintered areas, while low-density regions indicate unsintered powder. Point 1, marked on this plot, represents the location for which the density evolution over time is shown in the right plot. Here, the results demonstrate that the density increase occurs over a period of approximately $t = 35\,\mathrm{ms}$.

4.1.2. Part Scale

Similar to the micro-scale model, the results of the part-scale model, described in section 3, are presented below. The temperature results for the continuous model are shown in Figure 10.

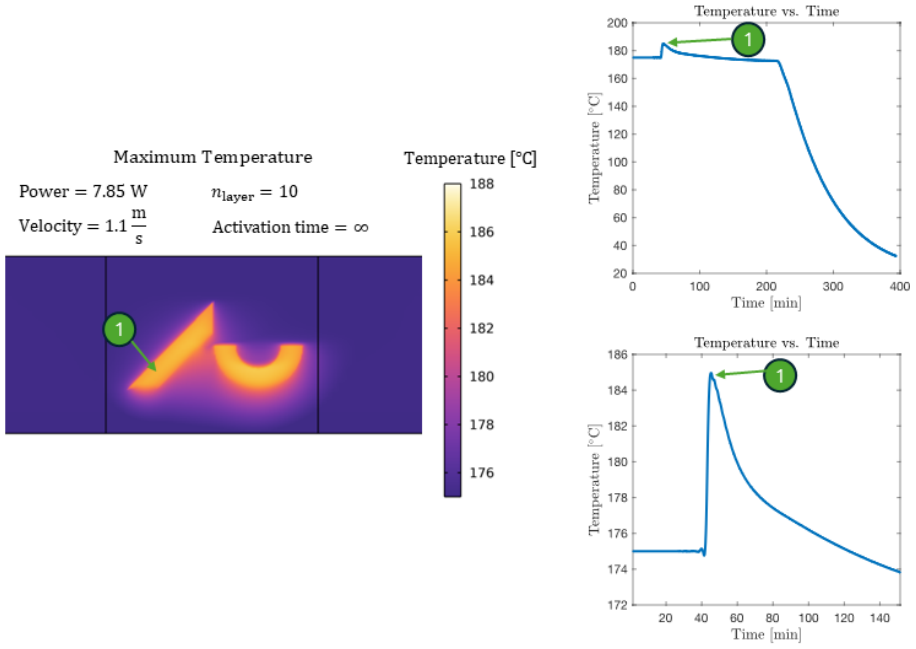

Figure 10: Temperature results for the continuous part-scale model.

On the left-hand side of Figure 10, the maximum temperature distribution on the plane is displayed. It can be observed that most of the plane remains close to the initial temperature of $T_0 = 175°\mathrm{C}$. However, in the region where the laser has been activated, the temperature reaches a peak of $T = 185°\mathrm{C}$. In the vicinity of the printed part, a slight temperature increase is noticeable, though clear thermal gradients are still observed, distinctly highlighting the shape of the printed part.

To illustrate the temperature evolution over time, the right-hand side of Figure 10 presents the temperature versus time at the point marked as 1. The top plot shows the temperature evolution for the entire printing process, including the cooling phase.

The bottom plot focuses on the temperature rise in greater detail, as this phase is not adequately resolved in the top plot. It can be seen that the temperature steadily increases over $t \approx 200\,\mathrm{s}$ before beginning its return towards the initial temperature.

A comparison can be made with the micro-scale model results shown in Figure 8. In the micro-scale model, the peak temperature reaches $T = 187.7°\mathrm{C}$ over a very short timescale of approximately $t \approx 1\,\mathrm{ms}$. In contrast, the continuous part-scale model exhibits a slightly lower peak temperature of $T = 185°\mathrm{C}$, which develops more gradually over $t \approx 200\,\mathrm{s}$. This slower heating rate at the part scale allows for more energy to migrate within the material, illustrating the differences in thermal behavior between the two scales.

In addition to temperature and density, the evolution of specific heat capacity is plotted as a function of temperature in Figure 11. The plot demonstrates how the specific heat capacity begins to rise as the temperature approaches the onset of melting at $T_{ms} = 176°\mathrm{C}$. This is to account for the absorption of latent heat during the melting process. During cooling, the specific heat capacity drops down as expected, waiting to release the latent heat until the onset

of solidification T_{ss} is reached. At this point, the same amount of latent heat that was absorbed during melting is released, confirming that the hysteresis model performs as intended.

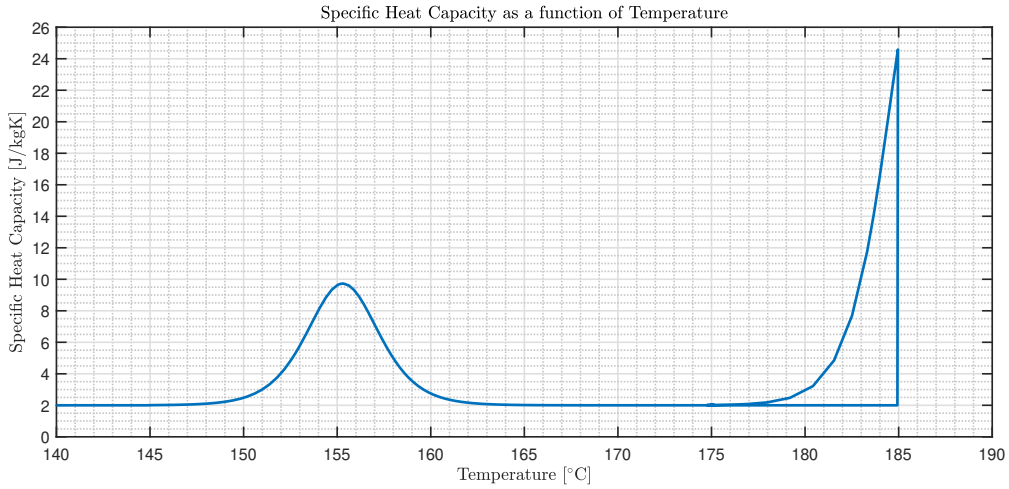

Figure 11: Specific heat capacity plotted as a function of temperature.

To mitigate the difference between the micro- and part-scale models, the part-scale model described in section 3 has also been simulated non-continuously with an activation time of $t_{\text{on}} = 40\,\text{s}$. The results of this simulation are presented in Figure 12.

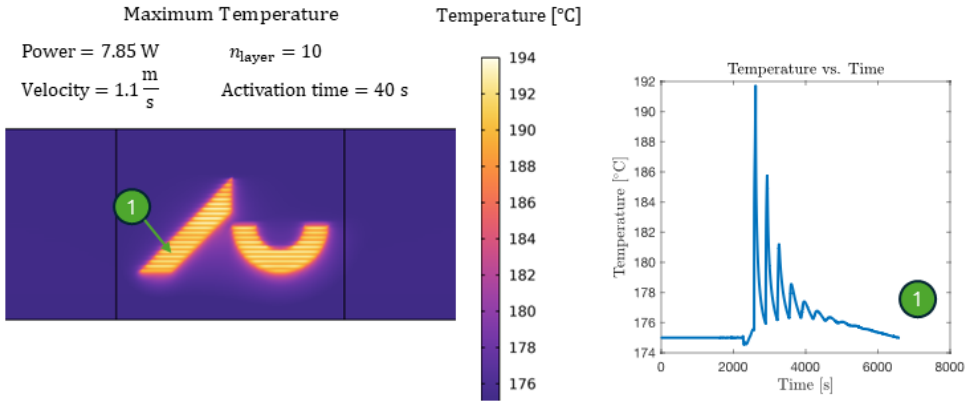

Figure 12: Temperature results for the part-scale model with an activation time of $t_{\text{on}} = 40\,\text{s}$.

On the left-hand side of Figure 12, the maximum temperature distribution on the plane is shown. Similar to Figure 10, the printed part is clearly visible, and most of the plane remains near the initial temperature. Horizontal bands of oscillating maximum temperature appear in the printed region due to the heat distribution of the laser being modeled as a Gaussian pulse moving incrementally upward in space.

The temperature evolution over time for the point marked as 1 is presented on the right-hand side of Figure 12. The temperature rises to a peak of $192°\text{C}$, higher than the $185°\text{C}$ observed in the continuous model (Figure 10). This increase occurs because the thermal energy is deposited over a shorter duration, allowing less time for energy dissipation. Specifically, the temperature rise occurs over $t = 40\,\text{s}$, closer to the $t = 1\,\text{ms}$ observed in the micro-scale model, though still much longer. Despite this, the peak temperature of $192°\text{C}$ in the part-scale model exceeds

the $T = 187.7°\mathrm{C}$ observed in the micro-scale model. This suggests reduced energy migration in the part-scale model compared to the micro-scale model. This will be further discussed in subsection 4.4.

After reaching the peak temperature, the temperature quickly drops but only briefly, as subsequent layer heating begins to influence the observed layer. This pattern repeats across multiple layers, with the magnitude of oscillations decreasing progressively.

Similarly to the temperature results, the density results for the part-scale model, with an activation time of $t_{\text{on}} = 40\ \text{s}$, are presented in Figure 13.

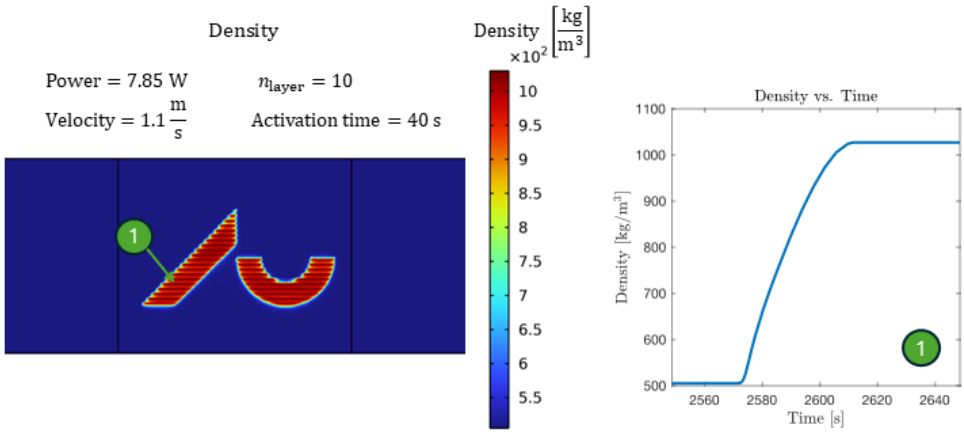

Figure 13: Density results for the part-scale model with activation time of 40 s.

The left-hand side of Figure 13 shows the density distribution in the plane, at the end of the simulation. It is evident that the part has been successfully sintered, as its density closely matches that of the solid material, ρ_{solid}, while the surrounding region retains the bulk density, ρ_{bulk}. The appearance of horizontal bands in the density plot can be attributed to the heat distribution being modeled as a Gaussian pulse.

On the right-hand side of Figure 13, the density evolution over time is shown for the point marked as 1. The plot demonstrates a clear increase in density from the bulk value to the sintered material density, occurring over the laser activation time t_{on}. This confirms that the temperature fluctuations observed after the initial peak in Figure 12 have no significant effect on the density evolution in the model.

4.2. Parameter Studies

This section focuses on conducting parameter studies to evaluate the influence of two key parameters: the activation time (t_{on}), which determines how long the laser remains on during each cycle, and the number of layers (n_{layer}), which specifies how many actual layers are simulated as one layer in the model. These parameters play a critical role in shaping the temperature and density distributions in the model, and understanding their impact is essential for improving the accuracy of the model.

4.2.1. Activation Time

The activation time of the laser, t_{on}, was defined in subsubsection 3.1.5. For this study, the temperature variation at a single point over time was analyzed for $t_{\text{on}} = 400\ \text{ms}$, $t_{\text{on}} = 40\ \text{s}$, and $t_{\text{on}} = \infty$ (continuous laser operation). With $n_{\text{layer}} = 10$ actual layers simulated simultaneously used. The results are presented in Figure 14.

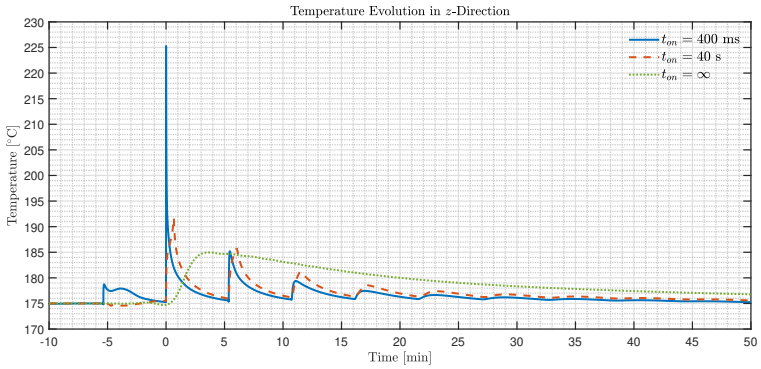

Figure 14: Temperature variation for different values of t_{on}.

From Figure 14, it is evident that the activation time t_{on} significantly influences the temperature peaks: shorter activation times result in higher temperature peaks. This behavior aligns with expectations, as the same energy is delivered, but over a reduced time frame, reducing time for energy dissipation.

Interestingly, in the non-continuous cases, the temperature difference between $t_{\text{on}} = 400$ ms and $t_{\text{on}} = 40$ s diminishes after the first peak. In the continuous model, the temperature curve remains smooth. Although the continuous case does not achieve the high peak temperatures observed in the non-continuous cases, it reaches temperatures comparable to those in the non-continuous cases after the first peak.

To further investigate the effect of activation time, Figure 15 presents the maximum temperature as a function of t_{on}.

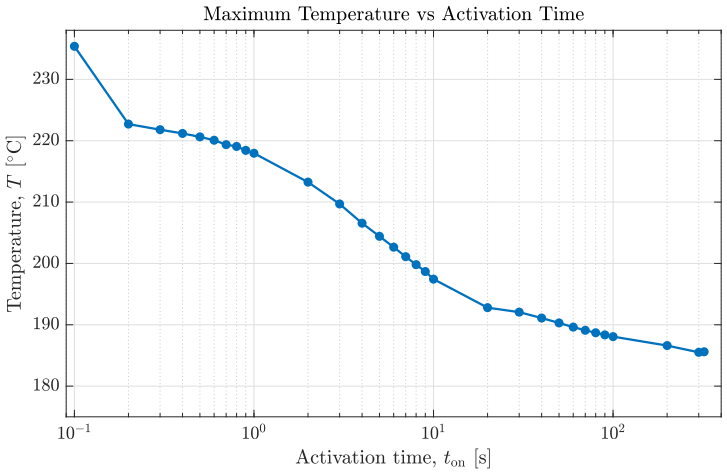

Figure 15: Maximum temperature as a function of activation time t_{on}.

Figure 15 clearly demonstrates that the maximum temperature increases as t_{on} decreases. As t_{on} becomes very small, it is expected that the maximum temperature will reach a plateau, as minimal energy is lost before the deposition is complete. A plateau-like behavior begins to emerge for $t_{\text{on}} < 1$ s. However, the result for $t_{\text{on}} = 0.1$ s deviates from this trend, likely due to numerical instabilities at such small activation times. Furthermore, it appears that the part-scale model at $t_{\text{on}} < 20$ s exceeds the maximum temperature of $T = 187.7°\text{C}$ observed in the micro-scale model by a significant margin, despite the faster energy transfer in the micro-scale model at $t \approx 1$ ms. This

further suggests that energy migration in the part-scale model is reduced in comparison to the micro-scale model. Which will be discussed in subsection 4.4.

4.2.2. Fusion of Layers

Multiple actual layers can be modeled as one, to make the model faster. A parameter study is now performed to determine how the number of fused layers, n_{layer}, affects the temperature at a single point over time. For this study, it has been chosen to investigate $n_{\text{layer}} = 5$, $n_{\text{layer}} = 10$, and $n_{\text{layer}} = 20$, all cases with $t_{\text{on}} = n_{\text{layer}} \cdot 4\,\text{s}$, to keep the compensation factor, η_D, constant. The results are plotted on the figure below.

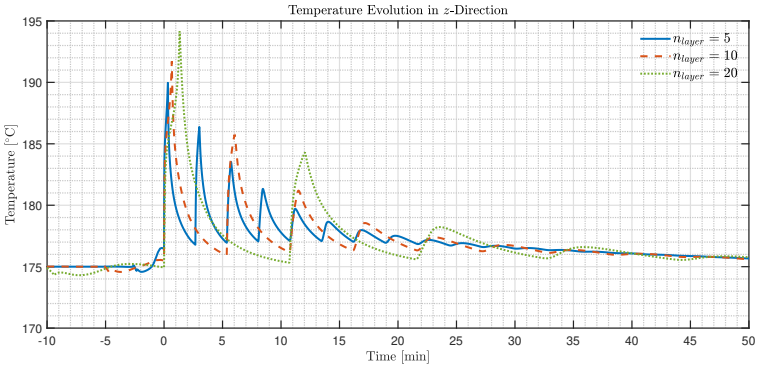

Figure 16: Parameter study of n_{layer}.

As expected, the plot demonstrates that the temperature profiles exhibit more peaks as the number of layers per heating cycle, n_{layer}, decreases. Specifically, $n_{\text{layer}} = 5$ has twice as many peaks as $n_{\text{layer}} = 10$ and four times as many peaks as $n_{\text{layer}} = 20$. Additionally, the temperature peaks become progressively wider as n_{layer} increases. This dissimilarity ensures that the compensation factor η_D in the analysis remains consistent.

Focusing on the first peak, the maximum temperature is slightly lower as n_{layer} decreases, suggesting that energy migration is slightly higher when the layer thickness is smaller.

Beyond the initial peaks, the decrease in temperature as layers beyond the observed layer are heated can be seen to follow the same trend. The temperature profiles converge, and after $t \approx 35\ \text{min}$, the difference in temperature between the cases is within $T \approx 0.5°\text{C}$. This indicates that while the number of layers per heating cycle significantly influences the short-term temperature behavior, the long-term temperature stability remains unaffected, with all cases reaching the same final temperature.

4.3. Extension from 2D to 3D Modeling

The part-scale model described in section 3 can easily be extended from 2D to 3D; however, this significantly increases the computation time, which is why the focus of this project has primarily been on the 2D case. However a 3D simulation was conducted, and the temperature results are presented in Figure 17. For this simulation, the continuous approach was chosen, with the amount of fused layers set to 20, to decrease computation time. A contour plot of the maximum temperature can be seen on the left, where it uniformly reaches $181°\text{C}$, which is $4°\text{C}$ lower than observed for the continuous 2D model in subsubsection 4.1.2.

On the right-hand side of Figure 17, the temperature evolution over time is plotted for the point indicated as 1, with the y-coordinate being in the middle of the printed structure. Here, it is observed that it takes $t \approx 40\ \text{min}$ for the temperature to return to the initial temperature after the maximum temperature of $T = 180.5°\text{C}$ has been reached. In comparison, the time it takes for the continuous 2D model, shown in Figure 10, to cool from $T = 180.5°\text{C}$

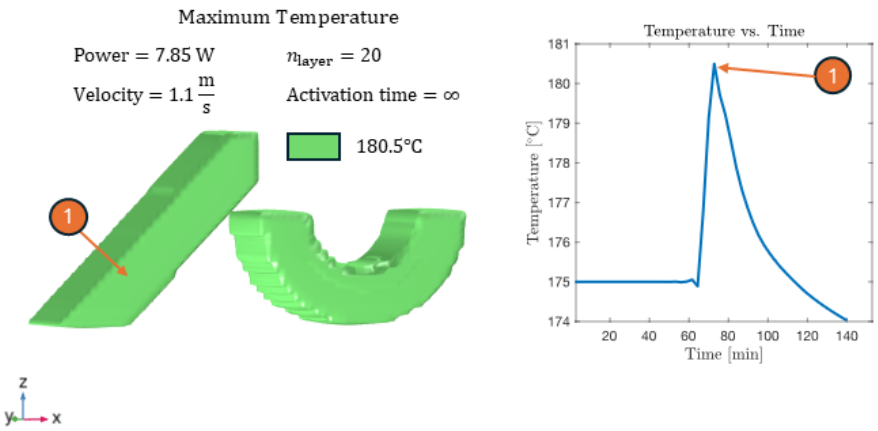

Figure 17: Continuous part-scale 3D model temperature results.

back to the initial temperature is measured to be $t \approx 65$ min. Thus, the 3D model cools down significantly faster than the 2D model. Which explain why the maximum temperature in the 3D simulation is lower than that of the 2D simulation. The faster heat dissipation in the 3D model causes more energy to dissipate before all the thermal energy is deposited into the material, preventing the material from reaching as high a temperature. This phenomenon is similar to the behavior observed in subsubsection 4.2.1, where a shorter activation time leads to higher temperatures.

4.4. Uncertainties

In this project, it was not possible to validate the temperature predictions with experimental observations. For the micro-scale model, an absorption coefficient of $K = 0.4$ was chosen based on experiments in the literature using similar powders [12]. For the part-scale model, an absorption coefficient of $K = 1$ was used, as the continuous model with this modification produced comparable, though slightly lower, temperature values. However, when the model was extended to a non-continuous approach, Figure 15 shows that the predicted temperatures at lower activation times significantly overestimate the values expected in the micro-scale model, which have a low activation time at $t_{on} \approx 1$ ms. This suggests that the absorption coefficient should be lower for the part-scale model. However, since the temperature results from the micro-scale model could not be validated, it is unclear whether these results are accurate enough to be used as a reliable guide. Future studies could address this limitation with additional resources and experimental data.

Some of the temperature discrepancies may also arise from the modeling assumptions. The use of a 2D model, which cools more slowly than a 3D model, likely contributes to these differences. Additionally, higher peak temperatures were observed when multiple layers were simulated as one, further impacting the discrepancies. Finally, the modeling approach appears to break down at activation times below $t = 0.1$ s. However, as Figure 15 suggests, a temperature plateau is reached before this time, indicating that the impact on the results may be minimal.

5. Conclusion

This study successfully developed and analyzed micro- and part scale models to predict the thermal behaviors of a sintering process.

At the micro-scale, rapid heating and cooling were observed, with peak temperatures reaching $T = 187.7$ °C over a timescale of approximately 1 ms. In contrast, the part-scale model exhibited slower heating rates, with

peak temperatures of $T = 185\ ^{\circ}\mathrm{C}$ for continuous operation and higher peaks for non-continuous simulations ($T = 192\ ^{\circ}\mathrm{C}$). These differences highlight the influence of energy migration and dissipation across modeling scales.

Parameter studies further highlighted the sensitivity of temperature distributions to laser activation time (t_{on}) and the number of fused layers (n_{layer}) in the part-scale model. Shorter activation times resulted in higher peak temperatures, while fewer fused layers resulted in lower temperature peaks. The choice of activation time influenced energy dissipation, with shorter durations limiting energy migration and leading to higher localized temperatures.

Extending the part-scale model from 2D to 3D revealed faster heat dissipation in three dimensions, resulting in lower peak temperatures. This indicates the importance of dimensional considerations in accurately modeling heat transfer and thermal gradients. However, this came with increased computational costs.

The primary uncertainty in this study lies in the lack of experimental validation for temperature predictions. The choice of absorption coefficients introduces potential inaccuracies, particularly in the part-scale model, where predicted peak temperatures exceeded expected values for lower activation times. Modeling assumptions, such as the use of 2D simulations and the fusion of multiple layers, also contributed to discrepancies. Addressing these limitations in future work through experimental validation will enhance the reliability of the presented results.

In conclusion, the developed models provide a framework for understanding the thermal evolution in sintering processes. Despite the identified uncertainties, the findings contribute valuable knowledge toward a numerical framework for studying and optimizing the SLS process.

6. Bibliography

[1] S. C. Ligon, R. Liska, J. Stampfl, M. Gurr, R. Mülhaupt, Polymers for 3d printing and customized additive manufacturing, Chemical Reviews 117 (2017) 10212–10290.

[2] M. Bayat, C. G. Klingaa, S. Mohanty, D. De Baere, J. Thorborg, N. S. Tiedje, J. H. Hattel, Part-scale thermo-mechanical modelling of distortions in laser powder bed fusion – analysis of the sequential flash heating method with experimental validation, Additive Manufacturing 36 (2020) 101508.

[3] L. Dong, A. Makradi, S. Ahzi, Y. Remond, Three-dimensional transient finite element analysis of the selective laser sintering process, Journal of Materials Processing Technology 209 (2009) 700–706.

[4] R. Goodridge, S. Ziegelmeier, 7 - powder bed fusion of polymers, in: M. Brandt (Ed.), Laser Additive Manufacturing, Woodhead Publishing Series in Electronic and Optical Materials, Woodhead Publishing, 2017, pp. 181–204. URL: https://www.sciencedirect.com/science/article/pii/B9780081004333000075. doi:https://doi.org/10.1016/B978-0-08-100433-3.00007-5.

[5] C. H. Forsberg, Chapter 2 - heat conduction equation and boundary conditions, in: C. H. Forsberg (Ed.), Heat Transfer Principles and Applications, Academic Press, 2021, pp. 23–55. URL: https://www.sciencedirect.com/science/article/pii/B9780128022962000020. doi:https://doi.org/10.1016/B978-0-12-802296-2.00002-0.

[6] J. Hesselvig, R. T. Nygaard, M. K. Budzik, M. Sandberg, Efficient continuum-based modelling and analysis of polymer sls: Insights into particle sintering and densification in straight and corner scanning passes, Additive Manufacturing (2025).

[7] H. J., N. R.T., Studying SLS-Printing Through Multiphysics Thermal and Flow Analysis With Experimental Validation, Bachelor's thesis, Aarhus University, Aarhus, Denmark, 2024.

[8] N. Rudolph, F. Wolff-Fabris, T. Sommer, K. Wudy, R. Setter, J. Hofmann, A. Blaeser, A. Fritschen, C. Hofstetter, S. Schmölzer, F. Beckstein, D. Rapp, R. Sehling, Thermal Analysis and Rheology in Polymer Additive Manufacturing, version 1 ed., NETZSCH-Gerätebau GmbH, 2023.

[9] G. Scherer, Viscous sintering, in: K. J. Buschow, R. W. Cahn, M. C. Flemings, B. Ilschner, E. J. Kramer, S. Mahajan, P. Veyssière (Eds.), Encyclopedia of Materials: Science and Technology, Elsevier, Oxford, 2001, pp. 9536–9540. URL: https://www.sciencedirect.com/science/article/pii/B0080431526017253. doi:https://doi.org/10.1016/B0-08-043152-6/01725-3.

[10] J. D. Williams, C. R. Deckard, Advances in modeling the effects of selected parameters on the sls process, Rapid Prototyping Journal 4 (1998) 90–100.

[11] A. E. Tontowi, T. H. C. Childs, Density prediction of crystalline polymer sintered parts at various powder bed temperatures, Rapid Prototyping Journal 7 (2001) 180–184.

[12] P. Peyre, Y. Rouchausse, D. Defauchy, G. Régnier, Experimental and numerical analysis of the selective laser sintering (sls) of pa12 and pekk semi-crystalline polymers, Journal of Materials Processing Technology 225 (2015) 326–336.

[13] C. Padeste, S. Neuhaus, Chapter 2 - polymer-on-polymer structures based on radiation grafting, in: C. Padeste, S. Neuhaus (Eds.), Polymer Micro- and Nanografting, Micro and Nano Technologies, William Andrew Publishing, Oxford, 2015, pp. 11–41. URL: https://www.sciencedirect.com/science/article/pii/B9780323353229000024. doi:https://doi.org/10.1016/B978-0-323-35322-9.00002-4.

[14] COMSOL Multiphysics, How to use state variables in comsol multiphysics, n.d. URL: https://www.comsol.com/blogs/how-to-use-state-variables-in-comsol-multiphysics, accessed: 2024-12-28.

[15] O. W. contributors, Courant–friedrichs–lewy condition, n.d. URL: http://www.oilfieldwiki.com/wiki/Courant%E2%80%93Friedrichs%E2%80%93Lewy_condition, accessed: 2024-11-19.

[16] Sinterit, Pa12-industrial material's technical data sheet, 2022. https://sinterit.com/wp-content/uploads/2022/11/PA12-Industrial.pdf [Accessed 20-05-2024].

[17] Sinterit, Lisa X — sinterit.com, 2024. https://sinterit.com/3dprinters/lisa-x/ [Accessed 18-04-2024].

[18] E. Tikhomirov, M. Åhlén, N. Di Gallo, M. Strømme, T. Kipping, J. Quodbach, J. Lindh, Selective laser sintering additive manufacturing of dosage forms: Effect of powder formulation and process parameters on the physical properties of printed tablets, International Journal of Pharmaceutics 635 (2023) 122780.

[19] C. Li, S. E. Snarr, E. R. Denlinger, J. E. Irwin, M. F. Gouge, P. Michaleris, J. J. Beaman, Experimental parameter identification for part-scale thermal modeling of selective laser sintering of pa12, Additive Manufacturing 48 (2021) 102362.

[20] M. Bayat, Multi-Scale Multiphysics Simulation of the Thermo-Fluid-Metallurgical-Mechanical Conditions During Metal Additive Manufacturing, Ph.D. thesis, Technical University of Denmark, 2020.

[21] J. Bony, S. Citherlet, Numerical model and experimental validation of heat storage with phase change materials, Energy and Buildings 39 (2007) 1065–1072.